

Effect of interfacial structures on phonon transport across atomically precise Si/Al heterojunctionsZexi Lu¹, Nathaniel P. Smith,² Micah P. Prange,¹ Raymond A. Bunker,² John L. Orrell,² and Anne M. Chaka^{1,*}¹*Physical Sciences Division, Physical and Computational Sciences Directorate, Pacific Northwest National Laboratory, 902 Battelle Boulevard, Richland, Washington 99352, USA*²*Signature Science and Technology Division, National Security Directorate, Pacific Northwest National Laboratory, 902 Battelle Boulevard, Richland, Washington 99352, USA*

(Received 23 June 2021; accepted 27 July 2021; published 26 August 2021)

Phonons are important carriers of energy and information in many cryogenic devices used for quantum information science and in fundamental physics experiments such as dark matter detectors. In these systems phonon behaviors can be dominated by interfaces and their atomic structures; hence, there is increasing demand for a more detailed understanding of interfacial phonon transport in relevant material systems. Previous studies have focused on understanding thermal transport over the entire phonon spectrum at and above room temperature. At ultralow temperatures, however, knowledge is missing regarding athermal phonon behavior due to the challenge in modeling the extreme conditions in microscale, heterogeneous cryogenic systems, as well as extracting single-phonon information from a large ensemble. In this paper, we delineate the effects of interfacial atomic structures on phonon transport using a combination of classical molecular dynamics (MD) and phonon wave-packet simulations, to illustrate the consistency and differences between the ensemble- and single-phonon dynamics. We consider three single-crystal Si surface reconstructions— (1×1) , $(\sqrt{3} \times \sqrt{3})$ and (7×7) —and model both experimentally observed Si (1×1) /Al interfaces and hypothesized Si $(\sqrt{3} \times \sqrt{3})$ /Al and Si (7×7) /Al interfaces. The overall interfacial thermal conductance calculated from non-equilibrium MD shows that for the Si (1×1) /Al system, the presence of Al twin boundaries can hinder phonon transport and reduce thermal conductance by 2–12% relative to single-crystal Al; whereas the Si $(\sqrt{3} \times \sqrt{3})$ and (7×7) reconstructions can enhance it by 6–19%. Normal mode decomposition reveals that both the increase and decrease in conductance are related to inelastic phonon scattering. Single-phonon wave-packet simulations predict phonon transport properties consistent with non-equilibrium MD, while further suggesting that phonon polarization conversion is significant even when elastic transmission dominates, and that the interfacial structures have anisotropic impacts on atomic vibrations along different lattice directions. Our findings suggest avenues for achieving selective phonon transport via controlling interfacial structures of materials using atomically precise fabrication techniques, and that the phonon wave-packet formalism is a potentially powerful method for developing a detailed understanding of non-equilibrium phenomena in the low-temperature limit.

DOI: [10.1103/PhysRevMaterials.5.086002](https://doi.org/10.1103/PhysRevMaterials.5.086002)**I. INTRODUCTION**

Progress in quantum information science (QIS) [1,2] relies on improved understanding of quantum excitations as information carriers for precision measurements and as energy carriers that transfer heat, thus enabling the achievement and maintenance of ultralow working temperatures for devices [3,4]. Phonons are important heat carriers in all solid-state materials, can be used as probes of material structures and properties, and also function as important signal transducers in high-energy physics (HEP) experiments. To successfully utilize phonons in QIS and HEP devices for measurement and heat dissipation, we need to understand phonon scattering mechanisms, especially their interactions with interfaces and defects, which can dominate phonon transport more than the properties of the bulk materials at the nanoscale [5–8].

The majority of studies of phonons have highlighted their role as heat carriers in thermal transport, usually at and above room temperature [9]. According to the kinetic theory, the thermal conductivity $k = 1/3 \times C_v v_g \lambda$ depends on the phonon heat capacity C_v , group velocity v_g , and mean free path $\lambda = v_g \tau$ (and thus also the phonon scattering rate $1/\tau$). Matthiessen's rule suggests that phonon transport depends on the combination of all scattering mechanisms, including phonon-phonon scattering in bulk phase single-crystal materials [10–12], phonon scattering with inhomogeneities including defects and oxidation [13–15], and phonon scattering with interfaces including those between different materials such as heterojunctions [16,17], and those in the same material such as grain boundaries between different crystallographic orientations [18,19]. Direct experimental delineation of the relationship between phonon transport and the aforementioned factors in realistic systems is complicated by the presence of multiple types of inhomogeneities that can couple to each other in a complex nonlinear manner, as well as difficulties in characterization of defects and interfaces that are buried

*anne.chaka@pnnl.gov

inside the systems. Therefore, theoretical calculations and atomistic simulations can provide essential insights that complement experimental observations. Specifically, experiments have shown that while inhomogeneities generally reduce thermal conductivity in bulk materials [20], at the interface they can enhance the thermal conductance in certain configurations [21,22]. Findings from our prior modeling studies suggested that both phenomena are due to the same phonon scattering mechanism, which reduces the phonon mean free path in homogeneous materials but can bridge the phonon mismatch between different materials [23].

While the development in QIS devices is predicated by advanced manufacturing techniques [24] and our ability to approach ultralow temperatures [25], correspondingly there is also increasing demand on knowledge of quantum-level particle physics under extreme conditions. For example, in Super Cryogenic Dark Matter Search (SuperCDMS) detectors, the initial energy deposition in semiconductors will convert to lattice vibrations, which propagate as phonons and eventually cross an interface into metals to break the cooper-pairs and get detected [3]. Understanding the propagation and scattering of these athermal phonons generated during this process is crucial for interpretation of the measurements [26–29]. Advanced fabrication techniques have also made possible the realization of atomically precise micro/nanostructures [30,31], which further emphasizes single-particle behaviors that are susceptible to local atomic structures or surface conditions that are precisely controlled. Therefore, understanding how structural and chemical inhomogeneities at the atomic level affect individual-phonon transport across interfaces is essential for the design of new materials and devices. However, in previous studies usually it is the overall phonon transport properties, such as the interfacial thermal conductance, that are measured or predicted, while the detailed single-phonon scattering mechanism with atomic-level material structures is missing. The conditions at or above room temperature where phonons follow the Bose-Einstein distribution also deviate from the QIS domain where athermal phonons dominate, leaving the phonon transport mechanisms at ultralow temperatures generally less well-understood.

In this paper, we focus on one heterojunction that is widely used for QIS and HEP systems: the Si/Al interface, and investigate the effect of its atomic structures on phonon transport and the underpinning phonon scattering mechanism. Si exhibits several well-known surface reconstructions that introduce many interesting properties such as unique electron-surface phonon coupling [32,33]. However, the effects of these reconstructions on interfacial thermal transport in a heterojunction is not known. Recent developments in molecular beam epitaxy (MBE) have made possible the fabrication of atomically perfect Si/Al interfaces grown on Si substrates with different surface reconstructions [30,31], which sets the realistic reference for our simulations. We consider a total of four different interfaces, which are summarized in Table I. To determine the commonalities and differences between transport mechanisms for phonons from the entire spectrum and individual athermal phonons, we conduct both classical non-equilibrium molecular dynamics (NEMD) and phonon wave-packet simulations. NEMD is a powerful technique to understand thermal transport integrated over all atomic-

TABLE I. The four types of Si/Al interfaces considered in our study. “p” stands for “perfect” as in “perfect single crystal”, and “t” stands for “twin” as in “twin boundary”.

Name	Si surface	Al type	Note
Si(1 × 1)-Al _p	(1 × 1)	perfect single crystal	MBE grown
Si(1 × 1)-Al _t	(1 × 1)	twin boundaries	MBE grown
Si($\sqrt{3} \times \sqrt{3}$)-Al _p	($\sqrt{3} \times \sqrt{3}$)	perfect single crystal	hypothesized
Si(7 × 7)-Al _p	(7 × 7)	perfect single crystal	hypothesized

vibrational modes [34], which intrinsically includes all the phonon scattering mechanisms, both elastic and inelastic, and predicts reasonable thermal properties with well-developed interatomic potentials. The phonon occupation in classical MD deviates from quantum-mechanical theory, but can be refined by corrections for comparison with experiments [23,35]. We first calculate and compare the overall interfacial thermal conductance at 100 and 200 K for all four interfaces. It is noteworthy that NEMD requires a notable temperature gradient established across the simulation system, which makes it impractical to conduct such simulations in the milli-Kelvin range. Therefore, we choose two temperatures to illustrate the trend of thermal transport. In addition, NEMD can only predict overall thermal properties that are a summation of all phonons; thus, we also apply normal mode decomposition (NMD) to delineate the spectral heat flow for an overview of the phonon transport mechanisms. To approach the ultralow temperature limit and the corresponding details of single-phonon behaviors, we further apply the phonon wave-packet approach where atoms remain motionless except when excited by the wave packet. We analyze the phonon scattering mechanism through the resulting atomic-vibrational spectra and direction-resolved atomic kinetic energies.

II. METHODOLOGY

All the molecular dynamics (MD) simulations are performed using the LAMMPS package [36], which requires classical interatomic-pair potentials to describe interactions among all atoms. Several pair potentials were evaluated for Si and Si/Al interfaces, such as the Tersoff potential [37] and a recently-developed angular dependence potential (ADP) [38]. However, the Tersoff potential cannot describe Si-Al interactions, while the ADP cannot correctly reproduce the Si surface reconstructions. The modified embedded atomic method (MEAM) potential of Jelinek *et al.* [39] satisfies both our demands of correctly reproducing structures of the Si surface reconstructions (as is demonstrated in the Results and Discussion section) and being able to describe Si-Al interactions; thus, it is used for all pair-wise and many-body atomic interactions. Our previous study showed that the bulk Si phonon spectrum is stretched, and the cutoff frequency of 26 THz is over-predicted by 10 THz [23,40]. This leads to an overestimated population and thermal conductance of high-frequency Si phonons. Even so, the MEAM potential can reproduce the surface structures and formation energies of Si and Al with excellent accuracy, which are important for modeling such atomically precise interfaces. Therefore, we select

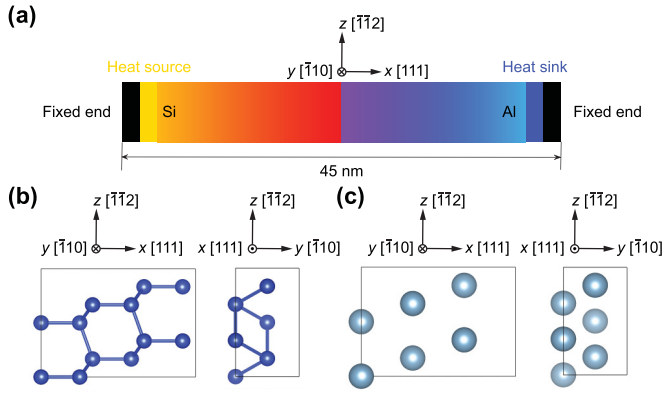


FIG. 1. (a) Illustration of the system domain for simulation. Heat is inserted in the source region at the left end of Si and is extracted from the sink region at the right end of Al; the temperature profile across the system provides an evaluation of the heat transfer performance. (b) Orthorhombic unit cell of Si consisting of 12 atoms, with its three vectors along $[1\ 1\ 1]$, $[\bar{1}\ 1\ 0]$, and $[\bar{1}\ \bar{1}\ 2]$, respectively. This unit cell serves as the monolithic building block to generate the Si blocks in our simulations by repeating itself along the three lattice vectors. (c) Same as (b) but for Al with 6 atoms.

the MEAM potential; its phonon-spectrum overestimation can be quantified and corrected using the approach described in our previous study [23], which considers deviations due to both the stretched phonon spectrum and the equipartition of energy phonon distribution [41]. The current paper focuses on investigating the effect of interfacial atomic structures on phonon transport using both NEMD and wave-packet simulations; therefore, for consistency we analyze the results without applying further adjustments.

A. Non-equilibrium molecular dynamics simulation and normal mode decomposition

A schematic of the system domain used for NEMD computation is shown in Fig. 1(a). The structure is periodic in all three dimensions. The single-crystal Si and Al blocks are of the same crystallographic orientations and joined through their $(1\ 1\ 1)$ planes, corresponding to the heterojunction grown by McSkimming *et al.* [30]. To facilitate building of the atomic structures, we define orthorhombic supercells of Si [12 atoms, Fig. 1(b)] and Al [6 atoms, Fig. 1(c)] with their three orthogonal lattice vectors along $[1\ 1\ 1]$ ($a_{\text{Si}} = 9.41\ \text{\AA}$, $a_{\text{Al}} = 6.98\ \text{\AA}$), $[\bar{1}\ 1\ 0]$ ($b_{\text{Si}} = 3.84\ \text{\AA}$, $b_{\text{Al}} = 2.85\ \text{\AA}$), and $[\bar{1}\ \bar{1}\ 2]$ ($c_{\text{Si}} = 6.65\ \text{\AA}$, $c_{\text{Al}} = 4.93\ \text{\AA}$). The Si block is 24-unit cells long while the Al block is 32-unit cells long, forming a 45-nm-long system with two materials of approximately the same length. The cross-sectional area, which is parallel to the interface, is specific for each of the four interfaces. For the two types of experimentally obtained Si/Al interfaces: Si (1×1) -Al_p (“p” stands for “perfect” as in “perfect single crystal”), and Si (1×1) -Al_t (“t” stands for “twin” as in “twin boundary”) with $(\bar{1}\ \bar{1}\ 2)$ Al twin boundaries, the cross section of our simulation box consists of 12×6 Si or 16×8 Al unit cells so that the interfacial lattice mismatch is small (1.2%). In the case of Si (1×1) -Al_t, we construct two twin boundaries in the simulation box as they must appear in pairs under pe-

riodic boundary conditions, resulting in a density of one twin boundary per $20.0\ \text{\AA}$. We also consider two additional types of Si/Al interfaces. Although the Si $(\sqrt{3} \times \sqrt{3})$ and (7×7) surface reconstructions are not preserved during the MBE growth and they eventually become (1×1) [30], they may be preserved by physically joining prefabricated Si and Al $(1\ 1\ 1)$ surfaces, and provide a useful hypothetical comparison. For Si $(\sqrt{3} \times \sqrt{3})$ -Al_p, we use the same simulation-box cross section as employed for the (1×1) reconstruction, because it can represent the surface reconstruction with two adatoms in every 3×2 boundary unit cells. For Si (7×7) -Al_p, a much larger cross section consisting of 21×21 Si or 28×28 Al unit cells is used to satisfy both the periodicity of the surface reconstruction (7×7 Si unit cells) and the Si/Al interfacial lattice mismatch (based on a three-to-four ratio). The cross sections of our modeling systems are large enough to eliminate the finite size effect, as they are at least four times the 4×4 Si $(1\ 0\ 0)$ unit cell area demonstrated to be sufficient by Landry and coworkers [42]. The length dependence of the interfacial thermal transport still exists, but extension to other lengths can readily be made using the linear extrapolation method introduced by Schelling and coworkers [43].

Thermal rectification has been demonstrated to exist at interfaces between materials of asymmetric thermal conductivities [44–46], as is true for our case. Here, we only consider the overall heat transfer from Si to Al as it more closely represents the phonon excitations and transport in cryogenic devices such as transition-edge sensors and quantum bits, which sets the background and focus for our study. Initially the system is relaxed in a constant number of atoms, pressure, and temperature (NPT) ensemble for 100 ps under zero pressure at the initial temperature (100 or 200 K). Then atoms in a region of $15\ \text{\AA}$ at both ends of the simulation domain are fixed to break periodicity in the heat transfer direction, and heat is inserted into a region of $15\ \text{\AA}$ adjacent to the fixed end of Si while it is extracted from a region of the same size next to the fixed end of Al, forming a constant heat flux J of $6.98 \times 10^9\ \text{W/m}^2$, which is consistently used for every simulation. It is noteworthy that the heat flux is large in order to generate distinct temperature differences across the interface for more facile analysis, consistent with our previous studies [23,47]. The simulation then proceeds in a constant number of atoms, volume, and energy (NVE) ensemble for 0.8 ns to reach steady state, and then another 6 ns for production. Temperature is averaged and recorded every $10\ \text{\AA}$ along the heat-transfer direction during the production run, from which the interfacial thermal transport efficiency is evaluated.

The NMD is based on the time domain normal mode analysis initially developed by Zhou and coworkers [48]. Here we apply the modified version as presented in our previous study [23]. The MD expression of heat flux (unit: W/m^2) is

$$J = \left\langle \sum_{ia} (E_{ia} \mathbf{v}_{ia} - \mathbf{S}_{ia} \mathbf{v}_{ia}) \right\rangle / V, \quad (1)$$

where ia refers to the atomic index, E is the total energy (potential and kinetic), \mathbf{S} is the Cauchy stress tensor, and V is the total volume [49–51]. Projection of the heat flux onto each phonon mode is then accomplished by expressing the atomic velocities using the time derivative of phonon normal mode

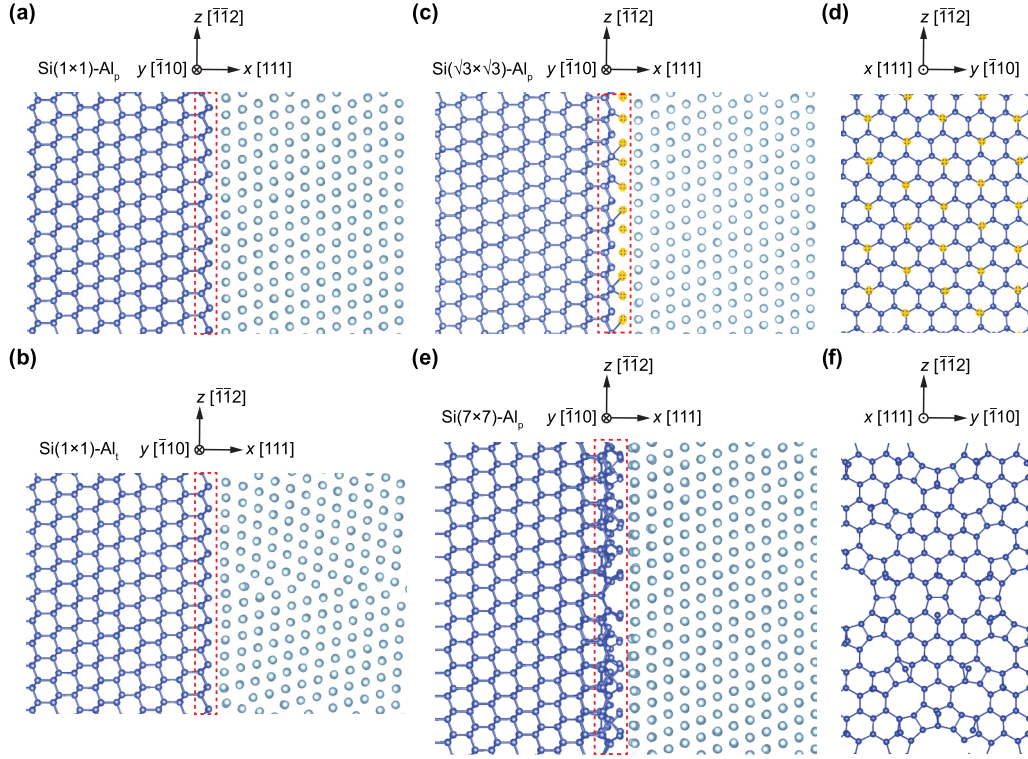


FIG. 2. Atomic structures of the $\text{Si}(1 \times 1)\text{-Al}_p$ (a), $\text{Si}(1 \times 1)\text{-Al}_l$ (b), $\text{Si}(\sqrt{3} \times \sqrt{3})\text{-Al}_p$ (c), and $\text{Si}(7 \times 7)\text{-Al}_p$ (e) interfaces obtained from our simulations. The red-dashed boxes indicate the boundary group of atoms selected for NMD analyses. (d) The view of boundary group atoms of the $\text{Si}(\sqrt{3} \times \sqrt{3})$ block along the $[\bar{1}\bar{1}\bar{1}]$ direction. Adatoms of the $\text{Si}(\sqrt{3} \times \sqrt{3})$ surface reconstruction are highlighted. (f) The same as (d), but for the $\text{Si}(7 \times 7)$ block. The structures of the $\text{Si}(1 \times 1)\text{-Al}_p$ and $\text{Si}(1 \times 1)\text{-Al}_l$ interfaces match perfectly with the experimental observations in Ref. [30]. The Si surface reconstructions are preserved at the hypothesized $\text{Si}(\sqrt{3} \times \sqrt{3})\text{-Al}_p$ and $\text{Si}(7 \times 7)\text{-Al}_p$ interfaces.

amplitude Φ :

$$\mathbf{v}_{jl,\mathbf{k},\nu,t} = \frac{1}{(Nm_j)^{0.5}} \mathbf{e}_{j,\mathbf{k},\nu} \exp(i\mathbf{k}\mathbf{r}_{jl}) \dot{\Phi}_{jl,\mathbf{k},\nu,t}. \quad (2)$$

where ν refers to the phonon branch, \mathbf{k} and \mathbf{r} are the trajectories in the reciprocal and real spaces, respectively, j and l refer to the j th basis atom in the l th unit cell, m is the atomic mass, N is the total number of unit cells, t is time, and \mathbf{e} is the phonon eigenvector. Compared with the original NMD [48], which uses the convoluted $\Phi_{\mathbf{k},\nu,t}$, our approach is specifically adjusted for applications to nonperiodic systems by further projecting Φ onto each atom:

$$\Phi_{jl,\mathbf{k},\nu,t} = \left(\frac{m_j}{N}\right)^{0.5} \mathbf{e}_{j,\mathbf{k},\nu}^* \exp(-i\mathbf{k}\mathbf{r}_{jl}) \mathbf{u}_{jl,t}, \quad (3)$$

where \mathbf{u} is the atomic displacement and \mathbf{e}^* is the complex conjugate of the corresponding phonon eigenvector.

To make clear distinctions among different cases, we apply NMD to interfacial atoms and choose only the surface layers of Si or Al atoms as the boundary groups for analyses. Each boundary group is treated as a single supercell evaluated at the Γ point only, where the phonon eigenvectors are acquired using the PHONON package [52] in LAMMPS for consistency with NEMD. For Al, this is always the first layer of boundary Al atoms (two atoms per boundary unit cell). For the $\text{Si}(1 \times 1)$ reconstruction, this is the first two layers of boundary atoms—four atoms per boundary unit cell, marked by red-dashed boxes in Figs. 2(a) and 2(b). The $\text{Si}(\sqrt{3} \times \sqrt{3})$

reconstruction has adatoms in addition to the boundary group of the (1×1) reconstruction, resulting in 26 atoms in every 3×2 boundary unit cells [red-dashed box in Fig. 2(c)]. The $\text{Si}(7 \times 7)$ reconstruction is more complicated. The dimer-adatom stacking fault (DAS) surface structure [53,54] has a period of 7×7 Si unit cells, and the cross section of our simulation domain contains nine of these repeatable structures. Still, the boundary group of the $\text{Si}(1 \times 1)$ reconstruction is present in the DAS structure, with some atoms removed or rearranged. Therefore, we choose all the atoms in the first two boundary layers plus those adatoms as the boundary group, resulting in 204 atoms per 7×7 Si boundary unit cells or 1836 atoms in the entire simulation domain [red-dashed box in Fig. 2(d)]. The trajectories, energies (potential and kinetic), and Cauchy stress tensors of the boundary group atoms are recorded during the NEMD production run, which are then used in NMD to calculate the spectral phonon heat flow.

B. Phonon wave-packet simulations

The phonon wave-packet methodology is especially suited to investigate single-phonon propagation and scattering mechanisms, as all atoms remain motionless except for those in the phonon wave packet. Such a simulation method provides a good approximation of the ultralow temperature regime in which the equilibrium thermal phonon population is exponentially suppressed. Here we apply the wave-packet approach initially developed by Schelling *et al.* [55,56]; the atoms are

displaced according to

$$\mathbf{u}_{jl} = A \cdot \mathbf{e}_{j\nu}(\mathbf{k}_0) \cdot \exp[i\mathbf{k}_0(\mathbf{x}_l - \mathbf{x}_0) - i\omega_\nu t] \cdot \exp[-\eta^2(\mathbf{x}_l - \mathbf{x}_0 - \mathbf{v}_{g\nu}t)^2]. \quad (4)$$

Here, \mathbf{u}_{jl} represents the displacement of basis atom j in the unit cell l located at \mathbf{x}_l , and $\mathbf{e}_{j\nu}(\mathbf{k}_0)$ is the eigenvector of the phonon with a wave vector of \mathbf{k}_0 from branch ν projected onto the same atom. The eigenvectors are also evaluated using the PHONON package for consistency with NEMD and NMD, as are the phonon frequency ω and group velocity \mathbf{v}_g . The wave packet is localized in space around \mathbf{x}_0 with a spatial extent of $\sim 1/\eta$. The initial atomic velocity can be found through the time derivative of Eq. (4):

$$\mathbf{v}_{jl} = \frac{\partial \mathbf{u}_{jl}}{\partial t} \Big|_{t=0} = \mathbf{u}_{jl}[-i\omega_\nu + 2\eta^2(\mathbf{x}_l - \mathbf{x}_0)\mathbf{v}_{g\nu}]. \quad (5)$$

Here we only consider phonons that are perpendicularly incident on the interface—effectively one-dimensional (1D) wave-packet simulations, as \mathbf{k} , \mathbf{x} , and \mathbf{v}_g are always along the same direction (Si [1 1 1]). We select η so that the wave packet is 20-Si unit cells long (~ 18.8 nm) along \mathbf{x} . This corresponds to a spread of $0.1(2\pi/a_{\text{Si}})$ around \mathbf{k}_0 in the reciprocal space. The amplitude A is selected so that the average energy E_{avg} inside the wave packet is 0.192, 0.384, or 3.84 meV/atom. The three different energies are used to represent the same phonons but of different populations, which can be correlated with their conditions at different temperatures. According to the equipartition of energy distribution [41], at any given temperature energy is evenly distributed among every phonon mode. Therefore, wave-packet simulations of different phonon modes but with the same E_{avg} are directly comparable as they correctly represent the phonon distribution at the same temperature. The 1D wave-packet simulations are performed for all four interfaces. With perpendicular incidence the cross section of the system becomes irrelevant. Therefore, we reduce the cross section to the smallest possible area, while expanding the length of the system to allow more space for phonon propagation. Each interface consists of a 60-unit cell long Si block and an 80-unit cell long Al block (~ 110 nm in total). The Si(1 \times 1)-Al_p and Si($\sqrt{3} \times \sqrt{3}$)-Al_p cases have cross sections of 3 \times 3 Si or 4 \times 4 Al unit cells, while that of the Si(1 \times 1)-Al_t case is 3 \times 6 Si or 4 \times 8 Al unit cells to ensure consistent density of twin boundaries with the NEMD simulations. The Si(7 \times 7)-Al_p interface has the same cross section as the NEMD simulation, which is already the smallest possible. The atomic structures are first fully relaxed at 10 mK, with periodic boundary conditions in all three dimensions and regions of 15 Å fixed at both ends, to generate an optimized system at an ultralow temperature. We select a series of phonon modes along the $\Gamma - \text{L}$ symmetry line based on the spectral heat flow and displace the atoms accordingly, which will be discussed in the Results and Discussion section. It should be noted that each simulation illustrates one phonon mode perpendicularly scattering with one interface. Initially the phonon wave packet is placed at a specific distance from the interface, which is chosen according to its modal group velocity, so that it needs to travel for at least 2.5 ps before scattering at the interface. The simulation proceeds for at least 15 ps to ensure that the transmitted

TABLE II. G_{int} of the considered interfaces at 100 and 200 K. ΔG_{int} is the percentage difference relative to the Si(1 \times 1)-Al_p result at the same temperature.

Temperature	Interface	G_{int} (GW/m ² K)	ΔG_{int}
100 K	Si(1 \times 1)-Al _p	0.2021	
	Si(1 \times 1)-Al _t	0.1767	-12.6%
	Si($\sqrt{3} \times \sqrt{3}$)-Al _p	0.2407	18.8%
200 K	Si(7 \times 7)-Al _p	0.2359	16.7%
	Si(1 \times 1)-Al _p	0.2502	
	Si(1 \times 1)-Al _t	0.2435	-2.7%
	Si($\sqrt{3} \times \sqrt{3}$)-Al _p	0.2985	19.3%
	Si(7 \times 7)-Al _p	0.2651	6.0%

and reflected phonons have sufficiently propagated away from the interface and can be separately identified. Some long-wavelength phonons will already be reflected a second time at the fixed ends during this period, but this part of the simulation is not used for analysis.

III. RESULTS AND DISCUSSION

A. Structures of Si/Al interfaces

An important test of classical MD simulations to ensure the classical force field is working properly is the resultant atomic structures of the materials. The relaxed interfacial structure [Fig. 2(a)] of Si(1 \times 1)-Al_p matches the experimental transmission electron microscope image in Ref. [30] perfectly, while that of Si(1 \times 1)-Al_t [Fig. 2(b)] shows more deformation. This originates from the substantially larger density of Al twin boundaries in our simulation (1/20.0 Å), which greatly amplifies their influence on atomic structures as well as phonon transport. However, in the simulated and experimental systems, the interfacial structures are qualitatively the same; therefore, we expect exaggerated yet consistent impact from the twin boundaries on the simulated phonon transport. For the Si($\sqrt{3} \times \sqrt{3}$)-Al_p [Fig. 2(c)] and Si(7 \times 7)-Al_p [Fig. 2(d)] cases, we first test the surface structures with a Si slab. We find that the MEAM potential can accurately reproduce the Si surface reconstructions. When the two hypothesized interfaces are formed (supposedly by pressing the prefabricated surfaces together), we find that the Si surface reconstructions are preserved in our simulations. Furthermore, the Al boundary atoms stay in their intrinsic lattice points. There is no obvious deformation or intermixing induced by the Si adatoms and the interfacial voids caused by them, which is consistent with the relatively high point-substitution energy (7.67 eV) for an Al atom in a Si host lattice as suggested by the MEAM potential [39].

B. Interfacial thermal conductance from NEMD simulations

The interfacial thermal conductance G_{int} (Table II) is calculated from the temperature profiles using the same method (Fig. 3) as in our previous study [23], where the linear temperature profile from the bulk phases of the materials are extrapolated to the interface to calibrate the temperature difference ΔT . The change in interfacial thermal conductance ΔG_{int} is calculated using the Si(1 \times 1)-Al_p case at the same

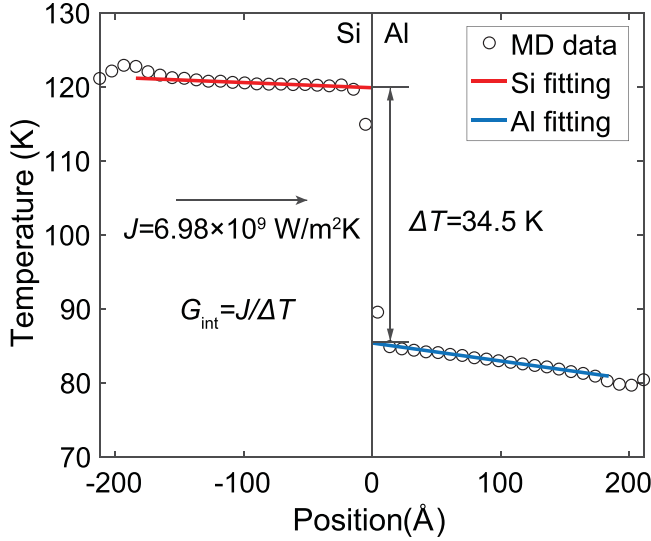


FIG. 3. Temperature profile of $\text{Si}(1 \times 1)\text{-Al}_p$ at 100 K from the NEMD simulation. The interfacial thermal conductance G_{int} is calculated from the difference in temperature ΔT across the Si/Al interface.

temperature as a reference. The Al twin boundaries are shown to reduce G_{int} compared with perfect single-crystal Al. A straightforward understanding is that the disorder introduced by the twin boundaries are hindering phonon transmission,

while the minimum interfacial intermixing is not sufficient to enhance phonon transport [57]. The reduction at 200 K (-2.7%) is smaller than at 100 K (-12.6%), which indicates that inelastic phonon transport, which becomes greater at higher temperatures, is likely making a significant contribution. In contrast, $\text{Si}(\sqrt{3} \times \sqrt{3})\text{-Al}_p$ and $\text{Si}(7 \times 7)\text{-Al}_p$ surprisingly show increased G_{int} despite the interfacial voids that reduce the effective contact area. We show below that this is mainly due to enhanced transport from Si phonons beyond the Al phonon cutoff frequency.

C. Spectral phonon transport from NMD

To further understand the phonon transport mechanism, we perform NMD on the boundary group of Si and Al atoms as selected in the Methodology section above (Fig. 2). The results are shown in Fig. 4 along with the corresponding phonon density of states (PDOS). We apply the autocorrelation technique [58,59] to calculate the PDOS,

$$D_{\alpha\beta}(\omega) = \int_0^\tau \Gamma_{\alpha\beta}(t) \cos(\omega t) dt, \quad (6)$$

where

$$\Gamma_{\alpha\beta}(t) = \frac{\langle \sum_{i_{\alpha\beta}=1}^{N_{\alpha\beta}} \mathbf{v}_{i_{\alpha\beta}}(t) \mathbf{v}_{i_{\alpha\beta}}(0) \rangle}{\langle \sum_{i_{\alpha\beta}=1}^{N_{\alpha\beta}} \mathbf{v}_{i_{\alpha\beta}}(0) \mathbf{v}_{i_{\alpha\beta}}(0) \rangle}. \quad (7)$$

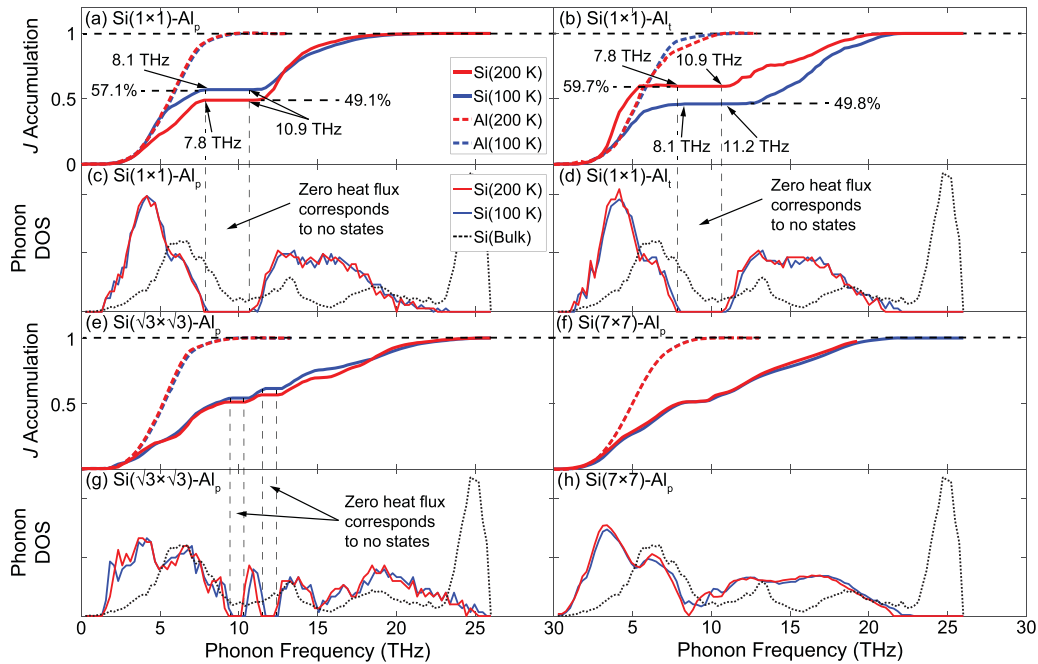


FIG. 4. Spectral heat flows J accumulation acquired from NMD for the $\text{Si}(1 \times 1)\text{-Al}_p$ (a), $\text{Si}(1 \times 1)\text{-Al}_t$ (b), $\text{Si}(\sqrt{3} \times \sqrt{3})\text{-Al}_p$ (e), and $\text{Si}(7 \times 7)\text{-Al}_p$ (f) interfaces. The corresponding PDOS of the Si atoms used to calculate J is plotted underneath each case, respectively [(c),(d),(g),(h)]. The dependence of J on temperature is clearly manifested at the $\text{Si}(1 \times 1)\text{-Al}_p$ and $\text{Si}(1 \times 1)\text{-Al}_t$ interfaces, while it is less significant at the $\text{Si}(\sqrt{3} \times \sqrt{3})\text{-Al}_p$ and $\text{Si}(7 \times 7)\text{-Al}_p$ interfaces. Plateaus are observed for interfaces with Si (1×1) reconstructions, and the PDOS reveals that this is caused by absence of phonon states within this frequency range. In contrast, this plateau feature is significantly reduced for interfaces with $\text{Si}(\sqrt{3} \times \sqrt{3})$ and (7×7) reconstructions, which show spectral heat flows that are almost temperature-independent. The $\text{Si}(\sqrt{3} \times \sqrt{3})\text{-Al}_p$ interface shows increment in cumulative J for phonons with frequencies higher than 23 THz that is consistent with available phonon states in this frequency range, which are absent at the other three interfaces.

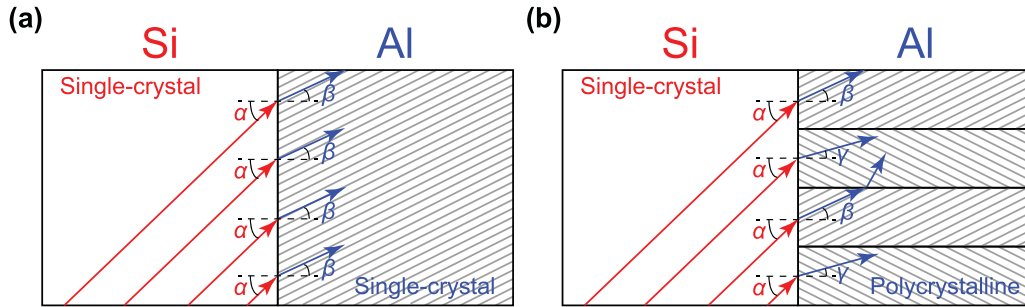


FIG. 5. Illustration of phonons of the same mode with the same incidence angle α scattering with the $\text{Si}(1 \times 1)\text{-Al}_p$ (a) and $\text{Si}(1 \times 1)\text{-Al}_t$ (b) interfaces, respectively. The two different grains of polycrystalline Al have different refraction angles β and γ , respectively. The transmitted phonons will collide with each other as their propagation directions are nonparallel.

Here $D(\omega)$ refers to the PDOS, t is time, ω is phonon frequency, i is the atomic index, α is the atom type, β is the region to which the atom belongs, $N_{\alpha\beta}$ is the total number of α atoms in region β , and \mathbf{v} is the atomic velocity. Equation (6) is evaluated over a period of time τ , which affects the frequency resolution of the spectrum and is ideally infinity. In our simulation we choose τ to be 25 ps, which equals a time step of 0.125 fs multiplied by 2×10^5 steps.

In the $\text{Si}(1 \times 1)\text{-Al}_p$ case [Fig. 4(a)], a plateau in the J accumulation curve appears for phonons from 7.8–10.9 THz, indicating that phonons in this range—high-frequency longitudinal acoustic (LA) and low-frequency longitudinal optical (LO) Si phonons—barely transfer heat across the interface. The Al cutoff frequency overlaps with this plateau region, beyond which the high-frequency Si phonons contribute more to G_{int} at 200 K (50.9%) than 100 K (42.9%), consistent with inelastic phonon scatterings being more significant at higher temperatures. The PDOS plot [Fig. 4(c)] reveals that there is no available phonon state in the Si boundaries within the plateau region. In bulk Si the LA phonons span from 0–16 THz and the LO phonons span from 16–26 THz, where they have modes with overlapping frequency at the boundaries of the first Brillouin zone. Consequently, there are available phonons across the entire 0–26 THz spectrum. However, in the boundary atomic layers with the $\text{Si}(1 \times 1)$ surface reconstruction, a gap of 7.8–10.9 THz opens between LA and LO phonons, resulting in the plateau in the J accumulation curve. The highest frequency optical phonons in bulk Si, represented by the peak around 25 THz in the PDOS plot, are also absent in the boundary and correspondingly there are more states within the 11–19 THz range. This explains the negligible spectral heat flow carried by phonons above 23 THz.

The $\text{Si}(1 \times 1)\text{-Al}_t$ case [Fig. 4(b)] shows an overall qualitatively similar curve with $\text{Si}(1 \times 1)\text{-Al}_p$. However, low-frequency (<5 THz) Si phonons below the Al cutoff show an opposite trend with a larger contribution to G_{int} at 200 K (59.7%) than 100 K (49.8%), and their spectral heat flow exceeds that of their Al counterparts at 200 K. This surprising phenomenon indicates inelastic scattering mechanisms that are specific to such interfaces with Al twin boundaries, where Si phonons are spontaneously combining into higher-frequency Al phonons when they cross the interface. We present an interpretation by investigating the elastic transmission from the perspective of the acoustic mismatch model [60], as illustrated in Fig. 5. When phonons of the same

mode are incident on the interface with the same angle α , they will have the same refraction angle β and travel in the same direction after the elastic scattering. However, if the Al is polycrystalline as it is in our case with twin boundaries, the same phonons incident on the grains with different crystallographic orientations will be scattered into different directions (refraction angles $\beta \neq \gamma$). Phonons that are spatially close before the interfacial scattering may quickly collide with each other and combine. Consequently, some of the elastic phonon transmission that occurs across the $\text{Si}(1 \times 1)\text{-Al}_p$ interface is converted to inelastic transport if twin boundaries are introduced in the Al lattice, because the boundaries can channel phonons into each other. Similar to all inelastic phonon scatterings, this phonon transport becomes more significant at higher temperatures, which explains the larger contribution from low-frequency Si phonons at 200 K.

The $\text{Si}(\sqrt{3} \times \sqrt{3})\text{-Al}_p$ and $\text{Si}(7 \times 7)\text{-Al}_p$ cases both show smoother J accumulation curves than the $\text{Si}(1 \times 1)$ cases, where the plateau feature is significantly reduced. In the $\text{Si}(\sqrt{3} \times \sqrt{3})\text{-Al}_p$ case [Fig. 4(e)] the Si phonons carry heat up to 25 THz, in contrast to other cases where the spectral heat flow becomes negligible beyond 22 THz. This is consistent with there being more phonon states available above 23 THz in the Si boundary with the $(\sqrt{3} \times \sqrt{3})$ surface reconstruction [Fig. 4(g)]. These observations indicate that both the $(\sqrt{3} \times \sqrt{3})$ and (7×7) surface reconstructions enable more channels for interfacial thermal transport from high-frequency LA and low-frequency LO Si phonons beyond the Al cutoff frequency, and the $(\sqrt{3} \times \sqrt{3})$ surface reconstruction further extends the additional channels to high-frequency Si optical phonons. The J accumulation curves at the two temperatures are surprisingly consistent for each of these two cases, indicating that the spectral heat flow is only slightly dependent on temperature and that high-temperature enhanced inelastic transport is probably negated by the simultaneously increased disorder in the surface adatoms. It is also noteworthy that the classical equipartition of energy distribution overestimates the population of high-frequency phonons, the extent of which becomes greater as temperature decreases. Therefore, the inelastic phonon transport at 100 K is overestimated to a greater extent than at 200 K. This contributes to the consistent spectral heat flow at both temperatures, which has been observed in classical MD simulations from previous studies [23,61], while in reality high-frequency Si phonons are expected to contribute more at 200 K.

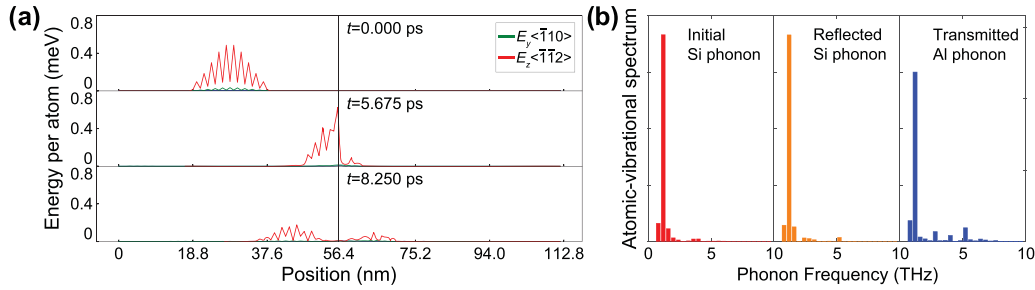


FIG. 6. (a) Illustrations of the TA-I phonon ($E_{\text{avg}} = 0.192$ meV) wave-packet propagation and scattering with the Si(1×1)-Al_p interface, represented by snapshots of the atomic kinetic energy at $t = 0, 5.675,$ and 8.250 ps. The kinetic energy at each position is averaged over all local atoms. (b) The corresponding atomic-vibrational spectra of the initial Si phonons, reflected Si phonons, and transmitted Al phonons.

D. Detailed interfacial scattering mechanism from single-phonon wave-packet simulations

While NMD is illustrative of the general phonon transport over the entire frequency spectrum, it cannot manifest the detailed phonon scattering mechanism. For example, it can tell whether a phonon in a certain frequency range transfers heat or not and how much it carries, but not what the phonon becomes after it goes across the interface. To explore the detailed scattering mechanism, we conduct phonon wave-packet simulations. Again, we only consider the incidence of Si phonons for consistency with the phonon excitations and transport in cryogenic devices. In addition, only in this way can we consider the scattering of phonons beyond the cutoff frequency of the material they are incident on, as Si has a broader spectrum than Al. Because the bulk phase of all Si blocks in our simulations are constructed by repeating the same Si 12-atom unit cell [Fig. 1(b)], we can initiate consistent Si phonon wave packets across all four interfaces. We select specific phonons based on the spectral heat flow from NMD, with eight phonons chosen from the four branches—LA, LO, transverse acoustic (TA), and transverse optical (TO)—that cover all critical ranges: the low-frequency range where $f < 5$ THz (LA-I, TA-I), the range below the Al cutoff frequency to which the Si(1×1)-Al_i case shows unique Si phonon inelastic scattering (LA-II, TA-II), the plateau in the Si(1×1)-Al_p case (LA-III), the slope after the plateau (LO-I, TO-I), and the highest-frequency optical phonon available (LO-II). All these phonons have the same reduced momentum of $\mathbf{k} = (0.25, 0, 0)$ in the folded first-Brillouin zone determined by the 12-atom unit cell. It should be noted that due to the specific phonon dispersion along $\Gamma - L$, not all branches are available in every range. For example, there is no transverse phonon in the same range with LA-III; so we only select phonons that are representative of their frequency range rather than trying to cover all possibilities. It is also noteworthy that many of these phonon modes are not pure longitudinal or transverse modes, and our classification is determined by examining the phonon eigenvectors according to the approach in Ref. [62].

The first 2.5 ps in the simulation before the phonon scatters with the interface is used to confirm the coherence of the phonons, namely that the phonon does not scatter into other phonons during propagation. We apply Eq. (6) again to calculate the atomic-vibrational spectrum. For a wave-packet simulation, the integral can only be performed over certain periods of time to correctly represent the phonons of interest. In our simulation a time step equals 0.125 fs, thus the first

2×10^4 steps representing $\tau = 2.5$ ps are used to characterize the initial phonon propagation. We find that the frequencies of all phonons remain consistent during propagation at all three energies during this period, except for LA-I, which breaks down when $E_{\text{avg}} = 3.84$ meV/atom and the corresponding result is not considered.

An example of the wave-packet simulation and the corresponding atomic-vibrational spectra are shown in Fig. 6, illustrating the TA-I phonon with $E_{\text{avg}} = 0.192$ meV/atom across the Si(1×1)-Al_p interface. The frequency and energy transmission of all eight selected phonons across the four interfaces are listed in Table III. Generally the results are consistent with NMD. For example, LA-III phonons have negligible transmission across the Si(1×1)-Al_p interface as the spectral heat flow forms a plateau at the frequency $f = 8.61$ THz, while it has increased transmission for the Si($\sqrt{3} \times \sqrt{3}$)-Al_p and Si(7×7)-Al_p interfaces as the plateau is absent. The wave-packet simulation reveals that the LA-III phonons are almost entirely reflected by the Si(1×1)-Al_p interface, but not the others. LA-III phonons also show a surprisingly increased transmission for the Si(1×1)-Al_i interface, which will be discussed later. When E_{avg} takes the two smaller values indicative of relatively small phonon population at low temperatures, elastic transmission dominates, and the LO-I phonon can hardly transfer energy across any interface. However, when E_{avg} takes the largest value, the LO-I phonon at elevated temperatures shows significantly enhanced inelastic transport across all four interfaces, which is consistent with the nonzero slope of the spectral heat flow curves at $f = 14.68$ THz. Details beyond NMD are also revealed. Compared with Si(1×1)-Al_p interfaces with Al twin boundaries or Si surface reconstructions reduce the transmission of low-frequency Si LA phonons, while they have varied effects on the TA phonons. Interfacial transport of LO phonons benefits from the Si surface reconstructions but not from the Al twin boundaries, whereas the TO phonons experience trivial impact as their ability to transfer energy into Al remains negligible.

By performing the vibrational spectrum analyses and distinguishing the atomic vibrations along all three directions, we gain more insight into the detailed phonon-interface scattering mechanism. We list the direction-resolved phonon vibrational energy in Table IV, where all energies are normalized by the total energy of their respective original Si phonon. Here we also elaborate on four phonon modes that most clearly manifest the differences among the four interfaces. Shown in Fig. 7 are the vibrational spectra of the LA-II phonon before

TABLE III. The frequency and energy transfer rate of the eight considered phonons across the four interfaces.

Frequency (THz)		Si(1 × 1)-Al _p			Si(1 × 1)-Al _t			Si(√3 × √3)-Al _p			Si(7 × 7)-Al _p		
E_{avg} (meV/atom)		0.192	0.384	3.84	0.192	0.384	3.84	0.192	0.384	3.84	0.192	0.384	3.84
LA-I	2.82	76.6%	67.2%		72.4%	63.0%		37.9%	33.1%		33.6%	28.7%	
TA-I	2.84	34.9%	33.0%	18.6%	37.3%	35.1%	28.6%	14.3%	15.9%	16.8%	46.4%	45.5%	36.5%
TA-II	6.03	9.5%	9.4%	7.5%	2.6%	2.6%	2.4%	0.4%	0.4%	0.3%	2.0%	1.9%	2.3%
LA-II	6.98	49.5%	48.6%	29.2%	41.1%	39.1%	30.3%	21.7%	21.7%	22.0%	14.5%	14.4%	13.7%
LA-III	8.61	0.8%	0.8%	1.4%	10.4%	10.5%	10.8%	7.5%	7.5%	9.3%	5.3%	5.3%	4.9%
LO-I	14.68	0.1%	0.2%	6.0%	0.2%	0.2%	5.2%	0.2%	0.2%	12.3%	0.2%	0.3%	10.0%
TO-I	16.23	0.0%	0.0%	0.0%	0.1%	0.1%	0.0%	0.1%	0.0%	0.0%	0.1%	0.1%	0.1%
LO-II	23.83	0.1%	0.2%	0.9%	0.2%	0.2%	1.2%	0.1%	0.2%	1.0%	0.3%	0.4%	7.3%

scattering with the interface, the reflected part, and the transmitted part. When $E_{\text{avg}} = 0.192$ meV/atom, we only show the Si(1 × 1)-Al_p case as there is no visible difference at the other interfaces. Elastic phonon transmission is observed for all four interfaces, and the detailed direction-resolved phonon vibrational energy shows significant polarization conversions [63], which indicates that the longitudinal and transverse atomic vibrations transform into each other during the scattering. When $E_{\text{avg}} = 3.84$ meV/atom, inelastic scattering becomes more significant as the LA-II phonons are reflected into several higher-frequency phonons by the interfaces, which have integer multiples of the frequency of the original Si phonon. This indicates that inelastic scatterings are dominated by linear combinations among the original phonons. The Al phonon wave packets show vibrational spectra with different frequency distributions from the initial Si phonons, also indicating inelastic phonon scattering, while elastic transmission still dominates as the majority of the phonons retain their original frequency.

The LA-III phonon shows significantly enhanced transport across interfaces with Al twin boundaries or Si surface re-

constructions at both $E_{\text{avg}} = 0.192$ and 3.84 meV/atom. The vibrational spectra (Fig. 8) show that, compared with the LA-II phonon, scatterings between the LA-III phonons and the interfaces are more consistently elastic at both energy levels as no phonons of other frequencies are manifested in the atomic-vibrational spectra, despite the LA-III phonon having much lower transmission. The direction-resolved kinetic energies reveal that the Al twin boundaries and Si surface reconstructions significantly enhance both polarization transmission and conversion. This trend seems to contradict the fact that a plateau of J accumulation is observed at the Si(1 × 1)-Al_t interface in this frequency range at 100 and 200 K. It is thus noteworthy that although we consider three different E_{avg} 's to represent phonons at different temperatures, each interface still has the same respective atomic structure optimized at 0 K across all simulations. Compared with the J accumulation curve at 200 K, the plateau is shifted towards high frequencies at 100 K; thus, we can expect the plateau to be shifted even further towards high frequencies at 0 K, which will likely result in a nonzero slope at $f = 8.61$ THz, and that the two methods are still consistent. However, one should note

TABLE IV. The direction-resolved kinetic energy distributions of the selected Si phonons before scattering with the interface and of the Al phonons that are generated from interfacial scattering. All energies are normalized by the total energy of their respective original Si phonon.

Mode and		Si(1 × 1)-Al _p			Si(1 × 1)-Al _t			Si(√3 × √3)-Al _p			Si(7 × 7)-Al _p		
E_{avg} (meV/atom)		E_x	E_y	E_z	E_x	E_y	E_z	E_x	E_y	E_z	E_x	E_y	E_z
LA-I	Si	100.0%	0.0%	0.0%									
	Al, 0.192	72.9%	1.9%	1.9%	62.9%	2.4%	7.2%	34.8%	1.7%	1.5%	18.5%	7.6%	7.5%
	Al, 0.384	62.1%	2.6%	2.6%	51.7%	3.2%	8.1%	29.0%	2.2%	1.9%	15.6%	6.6%	6.5%
LA-II	Si	89.0%	0.0%	11.0%									
	Al, 0.192	27.7%	7.4%	14.5%	15.9%	12.1%	13.0%	10.3%	6.3%	5.1%	6.8%	3.7%	4.0%
	Al, 3.84	14.9%	6.2%	8.1%	11.0%	9.3%	10.4%	9.9%	6.5%	5.6%	6.3%	3.5%	3.8%
LA-III	Si	87.2%	0.0%	12.8%									
	Al, 0.192	0.5%	0.2%	0.1%	4.2%	2.3%	4.0%	4.4%	2.7%	0.4%	2.1%	1.5%	1.7%
	Al, 3.84	0.9%	0.2%	0.2%	4.5%	2.5%	3.8%	4.5%	4.1%	0.8%	1.9%	1.4%	1.6%
LO-I	Si	100.0%	0.0%	0.0%									
	Al, 3.84	5.4%	0.3%	0.3%	3.3%	0.7%	1.2%	6.1%	3.1%	3.1%	4.1%	3.0%	2.9%
TA-I	Si	0.3%	6.8%	92.9%									
	Al, 0.192	2.7%	5.1%	27.1%	7.0%	8.1%	22.3%	0.2%	1.6%	12.5%	7.0%	7.4%	31.9%
	Al, 3.84	5.3%	5.4%	7.9%	6.9%	6.0%	15.7%	5.2%	5.7%	5.9%	6.7%	7.5%	22.4%
TA-II	Si	0.2%	91.6%	8.2%									
	Al, 0.192	3.4%	4.3%	1.8%	0.9%	0.9%	0.8%	0.2%	0.1%	0.1%	0.8%	0.7%	0.6%
	Al, 3.84	3.0%	3.0%	1.6%	0.8%	0.9%	0.7%	0.1%	0.1%	0.1%	0.8%	0.8%	0.7%

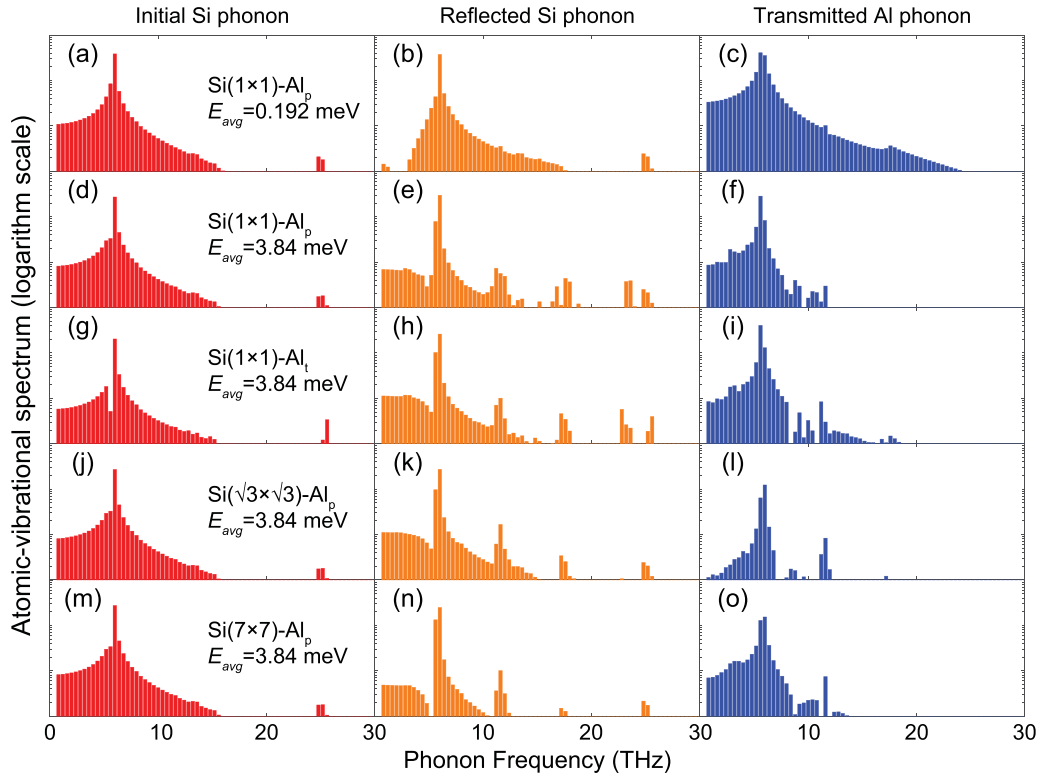


FIG. 7. The atomic-vibrational spectra (logarithm scale) acquired for the initial Si phonon, reflected Si phonon, and transmitted Al phonon from the LA-II phonon wave-packet simulations. The spread of frequency in the initial Si phonon results from the finite size truncation of the wave-packet's spatial span. All cases except the $\text{Si}(1 \times 1)\text{-Al}_p$ case with $E_{\text{avg}} = 0.192$ meV show significant inelastic phonon scattering, with peaks appearing in the vibrational spectra of the reflected phonon at frequencies that are integer multiples of the frequency of the incidence Si phonon (except for the peak at ~ 25 THz, which represents trivial fractions of unintended phonons resulting from inaccuracy of the eigenvectors of the original phonon).

this limitation of the wave-packet approach in representing high-temperature systems.

Lastly, we compare the two TA phonons. In addition to their different frequencies, their atoms are also vibrating in different planes: in the TA-I phonon atoms mainly vibrate in the $(\bar{1}10)$ plane, whereas the TA-II phonons mainly vibrate in the $(\bar{1}\bar{1}2)$ plane. Vibrational spectra (Fig. 9) show that for the TA-I phonon, elastic scatterings dominate at all four interfaces when $E_{\text{avg}} = 0.192$ meV/atom, while inelastic scatterings dominate when $E_{\text{avg}} = 3.84$ meV/atom. In contrast, the TA-II phonons (Fig. 10) elastically scatter with all four interfaces at both energies. Still, at the higher energy $E_{\text{avg}} = 3.84$ meV/atom a noticeable portion of the TA-II phonons experience inelastic scattering through linear combination, as is manifested by the second peak of the transmitted phonon at the frequency twice that of the original Si phonon in the vibrational spectra. The direction-resolved kinetic energy reveals that both phonons experience significant polarization conversion at the interface, except for TA-I phonons in the $\text{Si}(\sqrt{3} \times \sqrt{3})\text{-Al}_p$ case where the Al phonons are still vibrating largely along the initial directions. Comparing the LA-I and LA-II phonons, it is obvious that frequency can affect the phonon transport. In addition, we speculate that there is directional anisotropy in polarization conversion that can be linked to the interfacial structures. The comparison between TA-I and TA-II across the $\text{Si}(1 \times 1)\text{-Al}_p$ interface suggests that this type of interface is more amenable to transport of

vibrations in the $(\bar{1}10)$ plane than in the $(\bar{1}\bar{1}2)$ plane, which are perpendicular to each other. The other two surface reconstructions have the same symmetries with bulk Si and Al along $[111]$: C_3 rotation symmetry about the $[111]$ direction and mirror symmetry about the $(\bar{1}10)$ plane (Fig. 2). Consequently, there is no additional anisotropy confinement from the surfaces. Therefore, our results from Table IV indicate that the $\text{Si}(7 \times 7)$ reconstruction enhances the transport of $(\bar{1}10)$ plane vibrations, while further suppressing the $(\bar{1}\bar{1}2)$ plane vibrations. The $\text{Si}(\sqrt{3} \times \sqrt{3})$ reconstruction suppresses both, $(\bar{1}\bar{1}2)$ more so than $(\bar{1}10)$. The Al twin boundaries, on the other hand, destroy the C_3 rotation symmetry and introduces an additional mirror symmetry about the $(\bar{1}\bar{1}2)$ plane. The impact on phonon transport is similar with that of the $\text{Si}(7 \times 7)$ reconstruction, and we notice that they both have mirror symmetry about the $(\bar{1}10)$ and $(\bar{1}\bar{1}2)$ planes.

Compared with NEMD and NMD, the wave-packet simulations provide more details about the phonon scattering mechanisms, especially single-phonon behavior at ultralow temperatures. However, the 1D wave-packet simulation has its limitations because only perpendicular incidence is considered. Besides limiting the case studies, it also contributes to another issue with the analysis, as all phonon momentums are confined along the same line. While this may not impose any additional constraints on elastic transmission according to AMM, it suppresses inelastic scattering by eliminating

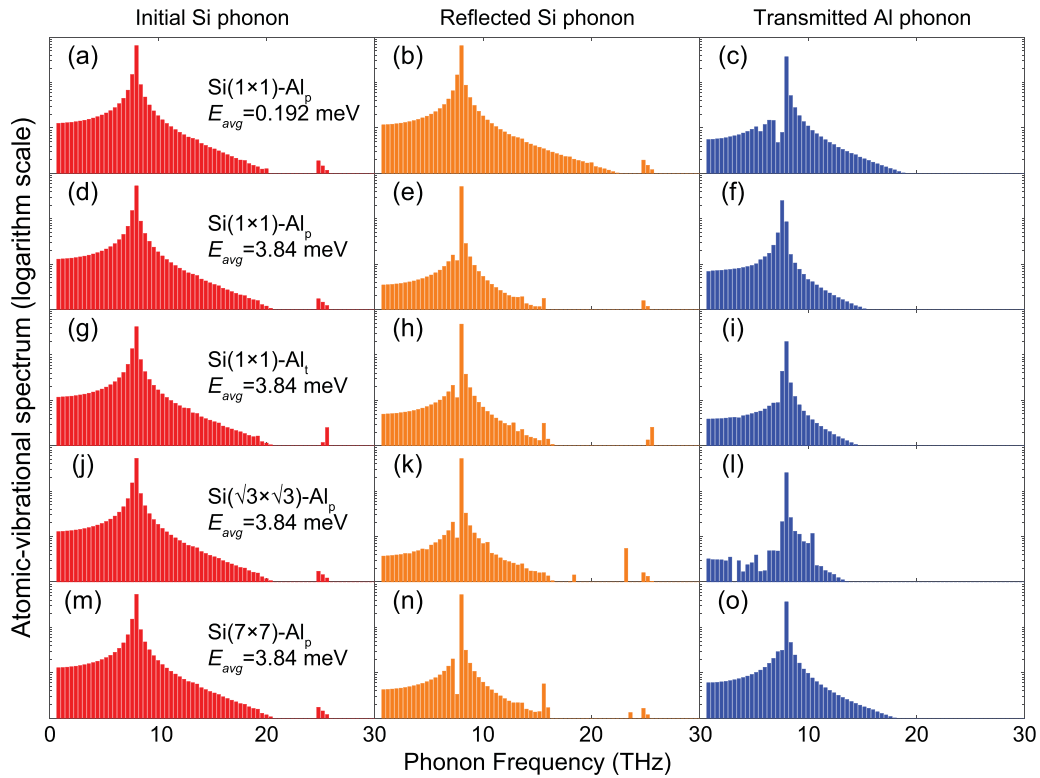


FIG. 8. Same with Fig. 7 but for the LA-III phonon. Compared with the LA-II phonon, the LA-III phonon shows more consistent elastic transmission at both energy levels for all four interfaces. It should be noted that in the $\text{Si}(1 \times 1)\text{-Al}_p$ cases the phonons are almost entirely reflected, but the low-transmission into Al is elastic.

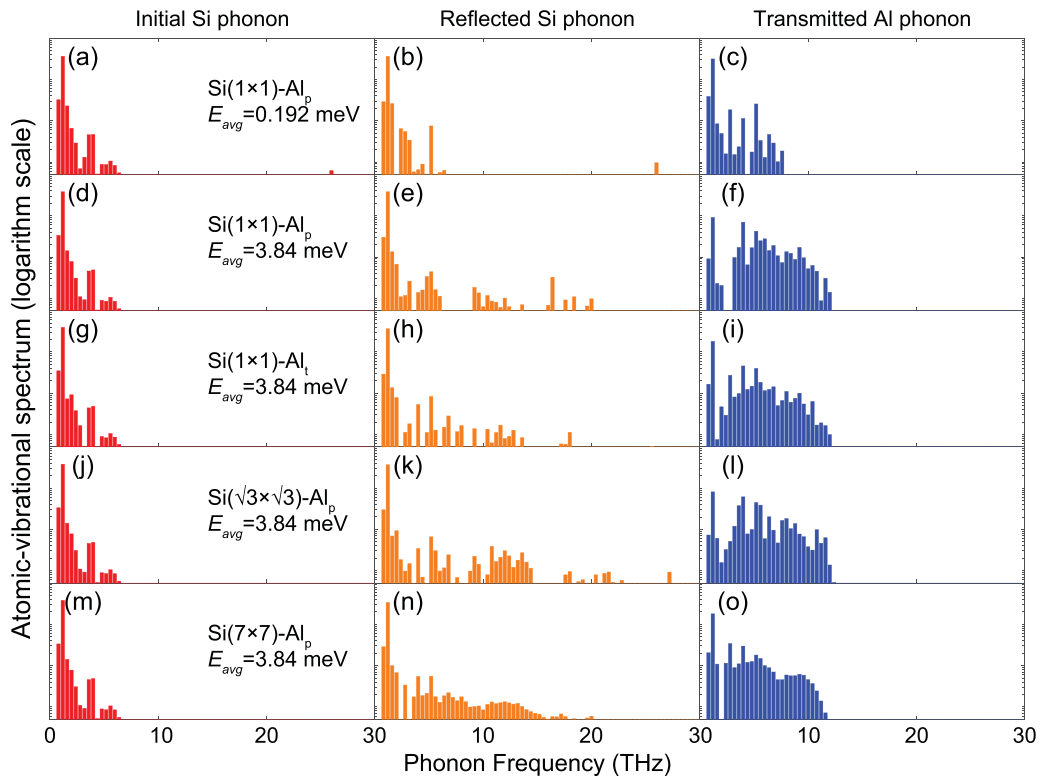


FIG. 9. Same with Fig. 7 but for the TA-I phonon. Inelastic scattering is significant for all four interfaces when $E_{\text{avg}} = 3.84$ meV.

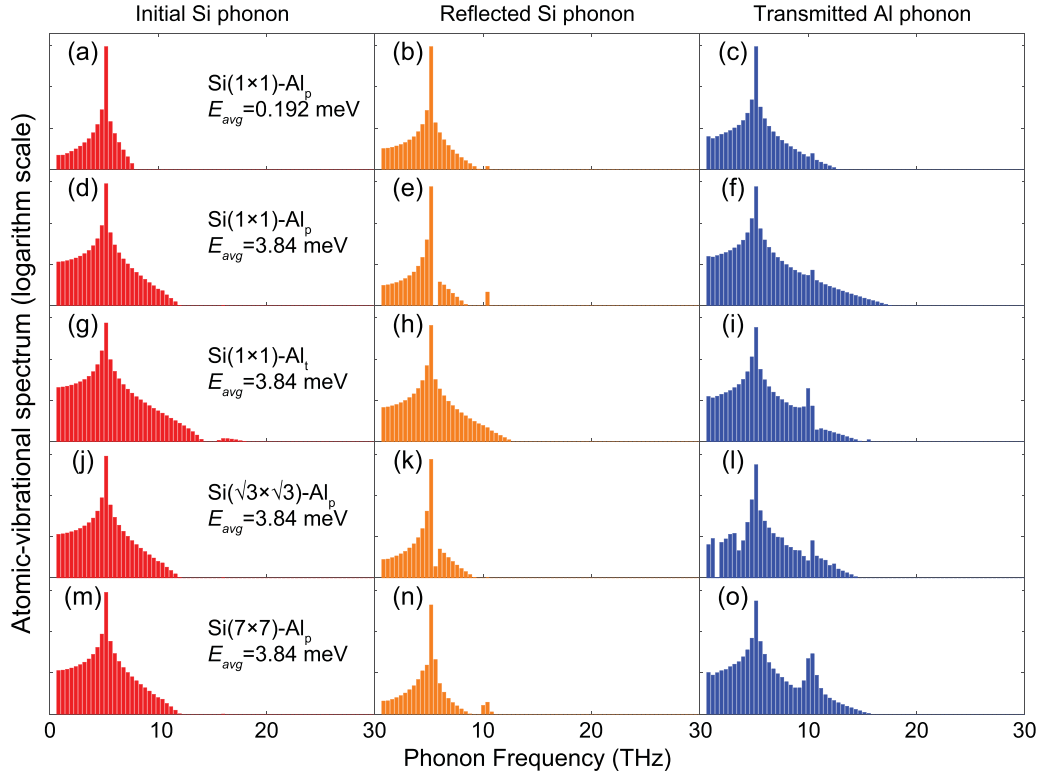


FIG. 10. Same with Fig. 7 but for the TA-II phonon. Compared with the TA-I phonon, the TA-II phonon shows more consistent elastic transmission at both energy levels for all four interfaces. A noticeable feature is that a second peak showing a frequency that is twice that of the original phonon appears for all four interfaces in the transmitted phonon when $E_{\text{avg}} = 3.84$ meV, which is most significant for the $\text{Si}(7 \times 7)\text{-Al}_p$ interface. This indicates collinear inelastic combination of the phonons.

all possibilities where the scattering phonons do not have collinear momenta. As a result, the elastic transmission may be overestimated, because the phonons are forced to transmit or get reflected if there is no allowed collinear inelastic transition. Still, the 1D approach is able to predict consistent trends with NEMD or NMD, which are methods that include all incident angles, and can provide more insights as demonstrated in our paper.

IV. SUMMARY

We have identified the influence on interfacial phonon transport from the structures across four atomically precise Si/Al interfaces— $\text{Si}(1 \times 1)\text{-Al}_p$, $\text{Si}(1 \times 1)\text{-Al}_t$, $\text{Si}(\sqrt{3} \times \sqrt{3})\text{-Al}_p$ and $\text{Si}(7 \times 7)\text{-Al}_p$ —and the detailed underlying phonon scattering mechanisms with a combination of NEMD, NMD, and single-phonon wave-packet simulations. The NEMD results at 100 and 200 K show that the Al twin boundaries reduce the interfacial thermal conductance by 12.6% and 2.7%, respectively, relative to the $\text{Si}(1 \times 1)\text{-Al}_p$ interface. In contrast, the $\text{Si}(\sqrt{3} \times \sqrt{3})$ and (7×7) reconstructions can enhance phonon transport by 18.8–19.3% and 6.0–16.7%, respectively. By conducting NMD, we reveal the spectral phonon heat flow, which shows that the Al twin boundaries are converting the elastic transmission of low-frequency Si phonons across the otherwise ideal interface into inelastic scattering by channeling the phonons into each other. The $\text{Si}(\sqrt{3} \times \sqrt{3})$ and (7×7) reconstructions, in contrast, enhance high-frequency Si phonon transport by providing more

channels for them to inelastically convert into Al phonons. To further approach the low-temperature context and reveal more details about the phonon scattering mechanism, we conduct phonon wave-packet simulations, compatible with the same system domains. Generally, NMD and wave-packet simulations show consistent results, while the latter provide more details showing that elastic transmission or reflection is predominant for Si phonons at low temperatures, while inelastic transport becomes more significant as the temperature increases. The significance of the inelastic scattering also depends on the phonon mode, because at the same temperature inelastic scattering is strong for some phonon modes, while it is negligible for others. By illustrating the direction-resolved atomic vibrations in the phonon wave packet, we find significant polarization conversion, which depends on temperature and interfacial structures. We find that the Al twin boundaries and Si surface reconstructions have anisotropic influence on the transport of atomic vibrations in the $(\bar{1}10)$ and $(\bar{1}\bar{1}2)$ planes. While the reference $\text{Si}(1 \times 1)$ reconstruction is more admissible to the former than the latter, the (7×7) amplifies this effect while $(\sqrt{3} \times \sqrt{3})$ in turn suppresses both. The effect of the Al twin boundaries is similar to the $\text{Si}(7 \times 7)$ reconstruction, and we speculate that this is related to the symmetries they have in common.

While certain limitations exist in our simulations regarding the classical phonon distribution and exaggerated density of twin boundaries, our model still predicts meaningful results that provide guidance. Further, more realistic approximations can be made by applying corrections to the phonon population

and linear interpolation to predict interfaces with a lower and more realistic density of twin boundaries. Despite these limitations, the results indicate that it should be possible to selectively control phonon transport via surface/interface engineering in real systems. While our ability to utilize phonons as probes of material properties, interfaces, and defects in QIS devices is predicated by our understanding of their scattering mechanism, it also in turn demands advanced design of experiments in the cryogenic domain that can provide more accurate measurements to deepen our knowledge. While it is currently impossible to directly simulate the long wavelengths representative of milli-Kelvin temperatures, we expect the trends extracted from modeling increasingly long-wavelength phonons will inform which types of interface properties (e.g., twin boundaries) will impact thermal conductance. We believe these results will lead to an increased understanding of thermal conductivity at ultra-low temperatures, especially when phonons interact with finite defects causing deviations from standard mismatch models. Comparison of experimental

measurements with well-controlled interfaces to trends from NEMD and single-phonon wave-packet simulations are crucial to understand the optimization of interfaces for devices. Our wave-packet approach is also well prepared to handle ultra-low temperature single-phonon physics, with the potential to be expanded to 2D for a greater modeling space.

ACKNOWLEDGMENTS

This work was supported by the Chemical Dynamics Initiative funded via Laboratory Directed Research and Development program at the Pacific Northwest National Laboratory (PNNL). PNNL is a multiprogram national laboratory operated by Battelle Memorial Institute for the U.S. Department of Energy. Computations for this paper were performed with Research Computing at PNNL and High Performance Research Computing (HPRC) at Texas A&M University (TAMU). Z.L., R.A.B., and A.M.C. thank Dr. David Toback from TAMU for providing support for HPRC.

-
- [1] X. Liu and M. C. Hersam, *Nat. Rev. Mater.* **4**, 669 (2019).
- [2] E. Sivre, H. Duprez, A. Anthore, A. Aassime, F. D. Parmentier, A. Cavanna, A. Ouerghi, U. Gennser, and F. Pierre, *Nat. Commun.* **10**, 5638 (2019).
- [3] R. Agnese, A. J. Anderson, T. Aramaki, I. Arnquist, W. Baker, D. Barker, R. Basu Thakur, D. A. Bauer, A. Borgland, M. A. Bowles, P. L. Brink, R. Bunker, B. Cabrera, D. O. Caldwell, R. Calkins, C. Cartaro, D. G. Cerdeño, H. Chagani, Y. Chen, J. Cooley *et al.* (SuperCDMS Collaboration), *Phys. Rev. D* **95**, 082002 (2017).
- [4] K. Y. Fong, H.-K. Li, R. Zhao, S. Yang, Y. Wang, and X. Zhang, *Nature (London)* **576**, 243 (2019).
- [5] E. Pop, S. Sinha, and K. E. Goodson, *Proc. IEEE* **94**, 1587 (2006).
- [6] D. G. Cahill, P. V. Braun, G. Chen, D. R. Clarke, S. Fan, K. E. Goodson, P. Keblinski, W. P. King, G. D. Mahan, A. Majumdar, H. J. Maris, S. R. Phillpot, E. Pop, and L. Shi, *Appl. Phys. Rev.* **1**, 011305 (2014).
- [7] P. Zhang, P. Yuan, X. Jiang, S. Zhai, J. Zeng, Y. Xian, H. Qin, and D. Yang, *Small* **14**, 1702769 (2018).
- [8] A. Giri and P. E. Hopkins, *Adv. Funct. Mater.* **30**, 1903857 (2020).
- [9] Q. Zheng, M. Hao, R. Miao, J. Schaadt, and C. Dames, *Prog. Energy* **3**, 012002 (2020).
- [10] T. Feng and X. Ruan, *J. Nanomater.* **2014**, 206370 (2014).
- [11] T. Feng, L. Lindsay, and X. Ruan, *Phys. Rev. B* **96**, 161201(R) (2017).
- [12] F. Tian, B. Song, X. Chen, N. K. Ravichandran, Y. Lv, K. Chen, S. Sullivan, J. Kim, Y. Zhou, T.-H. Liu *et al.*, *Science* **361**, 582 (2018).
- [13] T. Feng, X. Ruan, Z. Ye, and B. Cao, *Phys. Rev. B* **91**, 224301 (2015).
- [14] E. A. Scott, K. Hattar, C. M. Rost, J. T. Gaskins, M. Fazli, C. Ganski, C. Li, T. Bai, Y. Wang, K. Esfarjani, M. Goorsky, and P. E. Hopkins, *Phys. Rev. Materials* **2**, 095001 (2018).
- [15] B. Smith, L. Lindsay, J. Kim, E. Ou, R. Huang, and L. Shi, *Appl. Phys. Lett.* **114**, 221902 (2019).
- [16] A. Alkurdi, S. Pailhès, and S. Merabia, *Appl. Phys. Lett.* **111**, 093101 (2017).
- [17] X. Wei and T. Luo, *J. Appl. Phys.* **126**, 015301 (2019).
- [18] P. K. Schelling, S. R. Phillpot, and P. Keblinski, *J. Appl. Phys.* **95**, 6082 (2004).
- [19] S. Fujii, T. Yokoi, C. A. J. Fisher, H. Moriwake, and M. Yoshiya, *Nat. Commun.* **11**, 1854 (2020).
- [20] P. E. Hopkins, *ISRN Mech. Eng.* **2013**, 682586 (2013).
- [21] C. S. Gorham, K. Hattar, R. Cheaito, J. C. Duda, J. T. Gaskins, T. E. Beechem, J. F. Ihlefeld, L. B. Biedermann, E. S. Piekos, D. L. Medlin, and P. E. Hopkins, *Phys. Rev. B* **90**, 024301 (2014).
- [22] A. Giri, S. W. King, W. A. Lanford, A. B. Mei, D. Merrill, L. Li, R. Oviedo, J. Richards, D. H. Olson, J. L. Braun *et al.*, *Adv. Mater.* **30**, 1804097 (2018).
- [23] Z. Lu, A. M. Chaka, and P. V. Sushko, *Phys. Rev. B* **102**, 075449 (2020).
- [24] C. J. K. Richardson, N. P. Siwak, J. Hackley, Z. K. Keane, J. E. Robinson, B. Arey, I. Arslan, and B. S. Palmer, *Supercond. Sci. Technol.* **29**, 064003 (2016).
- [25] S. Friedrich, S. Boyd, and R. Cantor, Lawrence Livermore National Laboratory Report No. LLNL-TR-728645 (unpublished).
- [26] S. W. Leman, *Rev. Sci. Instrum.* **83**, 091101 (2012).
- [27] Y. Hochberg, M. Pyle, Y. Zhao, and K. M. Zurek, *J. High Energy Phys.* **01** (2016) 057.
- [28] R. K. Romani, P. L. Brink, B. Cabrera, M. Cherry, T. Howarth, N. Kurinsky, R. A. Moffatt, R. Partridge, F. Ponce, M. Pyle *et al.*, *Appl. Phys. Lett.* **112**, 043501 (2018).
- [29] S. Chigusa, T. Moroi, and K. Nakayama, *Phys. Rev. D* **101**, 096013 (2020).
- [30] B. M. McSkimming, A. Alexander, M. H. Samuels, B. Arey, I. Arslan, and C. J. K. Richardson, *J. Vac. Sci. Technol. A* **35**, 021401 (2017).
- [31] X.-Y. Liu, I. Arslan, B. W. Arey, J. Hackley, V. Lordi, and C. J. K. Richardson, *ACS Nano* **12**, 6843 (2018).
- [32] I. Barke, F. Zheng, A. R. Konicek, R. C. Hatch, and F. J. Himpsel, *Phys. Rev. Lett.* **96**, 216801 (2006).

- [33] M. Liebhaber, U. Bass, P. Bayersdorfer, J. Geurts, E. Speiser, J. Räthel, A. Baumann, S. Chandola, and N. Esser, *Phys. Rev. B* **89**, 045313 (2014).
- [34] E. S. Landry and A. J. H. McGaughey, *Phys. Rev. B* **80**, 165304 (2009).
- [35] J. E. Turney, A. J. H. McGaughey, and C. H. Amon, *Phys. Rev. B* **79**, 224305 (2009).
- [36] S. Plimpton, *J. Comput. Phys.* **117**, 1 (1995).
- [37] J. Tersoff, *Phys. Rev. B* **37**, 6991 (1988).
- [38] S. Starikov, I. Gordeev, Y. Lysogorskiy, L. Kolotova, and S. Makarov, *Comput. Mater. Sci.* **184**, 109891 (2020).
- [39] B. Jelinek, S. Groh, M. F. Horstemeyer, J. Houze, S. G. Kim, G. J. Wagner, A. Moitra, and M. I. Baskes, *Phys. Rev. B* **85**, 245102 (2012).
- [40] The Si phonon cutoff frequency measured by experiments is approximately 16 THz [64], which is accurately predicted by simulations using the Tersoff potential [37] and by first-principles calculations [65].
- [41] M. Puligheddu, Y. Xia, M. Chan, and G. Galli, *Phys. Rev. Materials* **3**, 085401 (2019).
- [42] E. S. Landry and A. J. H. McGaughey, *Phys. Rev. B* **79**, 075316 (2009).
- [43] P. K. Schelling, S. R. Phillpot, and P. Keblinski, *Phys. Rev. B* **65**, 144306 (2002).
- [44] N. Roberts and D. Walker, *Int. J. Therm. Sci.* **50**, 648 (2011).
- [45] Y. Wang, A. Vallabhaneni, J. Hu, B. Qiu, Y. P. Chen, and X. Ruan, *Nano Lett.* **14**, 592 (2014).
- [46] K. R. Hahn, M. Puligheddu, and L. Colombo, *Phys. Rev. B* **91**, 195313 (2015).
- [47] Z. Lu, Y. Wang, and X. Ruan, *Phys. Rev. B* **93**, 064302 (2016).
- [48] Y. Zhou, X. Zhang, and M. Hu, *Phys. Rev. B* **92**, 195204 (2015).
- [49] J. H. Irving and J. G. Kirkwood, *J. Chem. Phys.* **18**, 817 (1950).
- [50] T. Ohara, *J. Chem. Phys.* **111**, 9667 (1999).
- [51] D. Torii, T. Nakano, and T. Ohara, *J. Chem. Phys.* **128**, 044504 (2008).
- [52] L. T. Kong, *Comput. Phys. Commun.* **182**, 2201 (2011).
- [53] K. Takayanagi, Y. Tanishiro, M. Takahashi, and S. Takahashi, *J. Vac. Sci. Technol. A* **3**, 1502 (1985).
- [54] M. Smeu, H. Guo, W. Ji, and R. A. Wolkow, *Phys. Rev. B* **85**, 195315 (2012).
- [55] P. K. Schelling, S. R. Phillpot, and P. Keblinski, *Appl. Phys. Lett.* **80**, 2484 (2002).
- [56] C. Shao, Q. Rong, M. Hu, and H. Bao, *J. Appl. Phys.* **122**, 155104 (2017).
- [57] Z. Tian, K. Esfarjani, and G. Chen, *Phys. Rev. B* **86**, 235304 (2012).
- [58] J. M. Dickey and A. Paskin, *Phys. Rev.* **188**, 1407 (1969).
- [59] H. Bao, X. L. Ruan, and M. Kaviani, *Phys. Rev. B* **78**, 125417 (2008).
- [60] E. T. Swartz and R. O. Pohl, *Rev. Mod. Phys.* **61**, 605 (1989).
- [61] T. Feng, Y. Zhong, J. Shi, and X. Ruan, *Phys. Rev. B* **99**, 045301 (2019).
- [62] L. Cheng, C. Zhang, and Y. Liu, *J. Phys.: Materials* **2**, 045005 (2019).
- [63] J. Shi, J. Lee, Y. Dong, A. Roy, T. S. Fisher, and X. Ruan, *Phys. Rev. B* **97**, 134309 (2018).
- [64] J. c. v. Kulda, D. Strauch, P. Pavone, and Y. Ishii, *Phys. Rev. B* **50**, 13347 (1994).
- [65] S. Wei and M. Y. Chou, *Phys. Rev. B* **50**, 2221 (1994).